Available online at www.sciencedirect.com

ScienceDirect

Procedia CIRP 133 (2025) 555–560

www.elsevier.com/locate/procedia

20th CIRP Conference on Modeling of Machining Operations

Acceleration-based spindle monitoring based on geometric error motions

Aaron Cornelius*[a], Gregory W. Vogl[a], Ryan Hall[b], and Yongzhi Qu[b]

[a] *Engineering Laboratory, National Institute of Standards and Technology (NIST), 100 Bureau Drive, Gaithersburg, Maryland 20899-8220, USA (Official contribution of the National Institute of Standards and Technology; not subject to copyright in the United States.)*

[b] *Department of Mechanical Engineering, University of Utah, Salt Lake City, Utah 84112, USA*

* Corresponding author. Tel.: +1-301-975-8346. *E-mail address:* aaron.cornelius@nist.gov

Abstract

The development of intelligent machine tools requires integrating sensors that allow the machine to monitor, diagnose, and control the machining process. However, existing sensors for monitoring tool vibrations are intrusive and difficult to integrate in a production machining system. This paper describes how spindle-mounted accelerometers can be used to model spindle-speed dependent error motions *in situ*. It extends on previous work by applying a geometric model for interpreting tool holder displacements and spindle error motions from the motion of a laser that is coaxially mounted in a tool holder, providing an accurate and interpretable basis for training models that output geometric error motions via acceleration inputs. Trained data-driven models show the potential for use of spindle-mounted accelerometers to accurately estimate geometric error motions, even during spindle rotation with radial loads.

Keywords: Machine tool, Modeling, Monitoring

1. Introduction

In situ monitoring of machining operations and machine tool health is critical for producing quality parts. Traditional methods for measuring machine health require dedicated metrology setups which typically take the machine tool temporarily out of production [1]. Furthermore, these approaches generally measure the machine in a static state and ignore system changes during operation, such as shifts in spindle dynamics at high spindle speeds [2]. Ideally, the machine tool would monitor itself during normal operation, provide advance predictions for spindle failure, and measure its dynamics and vibrations to aid process optimization [3, 4].

However, the dirty nature of the work zone and the requirement to not interfere with machining operations can make it difficult to instrument the spindle [5]. Spindle-mounted accelerometers provide cost-effective and non-intrusive measurements of spindle vibration [6] and can be used for monitoring machine and process health [7-10]. The spindle vibrations also encode the spindle frequency response function (FRF) and provide information about the tool vibrations during cutting. However, existing studies for determining the FRF from spindle vibrations have had limitations. Zhou et al. calibrated spindle-mounted accelerometers using the static FRF, which ignores spindle-speed dependent FRF variations [11]. Postel et al. tap-tested a rotating tool at different speeds to capture these speed-dependent FRFs and vibrations, but this could pose safety concerns and is time-consuming to measure for many different spindle speeds [6]. Liu and Altintas instead learned the rotating FRF from stable and unstable cutting test vibrations [12, 13]. This required minimal instrumentation but is time-consuming and the unstable cuts can cause wear or damage to the tool and machine.

This paper describes data-driven models which estimate the rotating spindle error motions and FRF from accelerometer readings. A training data set was generated using a metrology

2212-8271
10.1016/j.procir.2025.02.095

suite which induced periodic forces on a rotating toolholder and measured the deflection of a spindle-mounted laser diode. The training data was processed with a geometric model to separate load and speed-induced error motions from pseudo-static machine/spindle errors. The processed training data was used to train physics-informed and XGBoost (XGB) [14] data-driven models which learn the spindle-speed dependent FRF. After training, the spindle can be monitored using the spindle-mounted accelerometers without any other instruments.

2. Experimental setup

Data for this work was collected using a custom metrology suite (Fig. 1a) which exerts controlled periodic forces on a rotating tool holder and measures the resulting tool deflections [15]. The rotating component of the suite was an instrumented tool holder which has a laser diode mounted coaxial to the spindle axis and a magnet embedded in the outside perimeter. The static measuring stage uses a pair of magnets to interact with the rotating tool to simulate periodic cutting forces of up to 200 N. The magnets are adjusted relative to the holder using linear stages to change the force magnitude, while instantaneous magnetic forces are measured by force-torque sensors (ATI Industrial Automation Mini45). The laser is split into two beams which project onto two laser position sensing modules (PSM 2-10 from On-Trak Photonics). The PSMs measure where the laser intersects the sensor plane within a 10 mm × 10 mm area and have a nominal resolution of 250 nm with 0.3% linearity over the full range. The position and orientation of the laser diode can be inferred from these sensor readings. The second laser path is elongated by bouncing the beam between two mirrors (Fig. 1b). This allows translational and rotational spindle deflections to be separated since only rotational deflections are scaled by the laser path length.

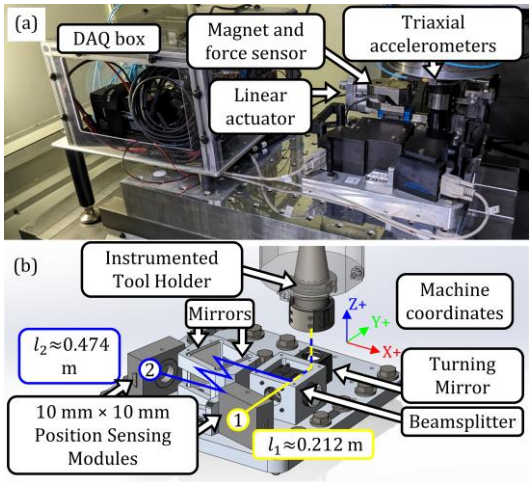

Fig. 1. (a) Experimental setup on the machine tool. The second magnet and force/torque sensor are hidden behind the spindle. (b) Metrology suite design model with highlighted laser paths with lengths l_1 and l_2. The reported lengths are with the spindle at $Z = 0$ mm. The magnet/force assemblies and optical covers have been hidden for clarity.

These measured forces and deflections are related to the accelerations measured from a pair of triaxial accelerometers superglued to the machine spindle housing. The testing for this work was performed on a Hurco VMX24 machining center.

3. Geometric modeling

Each PSM outputs two voltages, V_x and V_y, representing the position of the laser centroid in the sensor coordinate system. The geometric model predicts the voltage outputs for each PSM for a given machine position X, Y, Z in millimeters and spindle angle θ in radians. For simplicity, the sensors are represented as if they were directly in the laser path under the spindle, setting the sensor distance l to keep the same effective beam length. The bulk effects of the laser steering are lumped into the sensor alignment variables, while optical nonlinearities are considered by adding position and orientation dependent adjustments to the voltage coefficients. Fig. 2 shows the laser runout and machine alignment relative to the modeled sensor and Fig. 3 shows the orientation of the sensor itself.

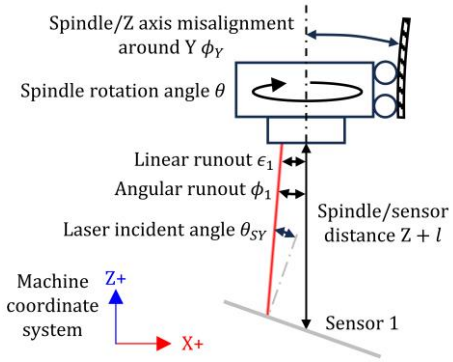

Fig. 2. Schematic of laser and machine alignment for a single PSM sensor based on the lumped orientation model. Laser runouts are expressed in the rotating coordinate system of the spindle. There is another set of runouts ϕ_2, ϵ_2 and spindle/Z-axis misalignments perpendicular to this figure.

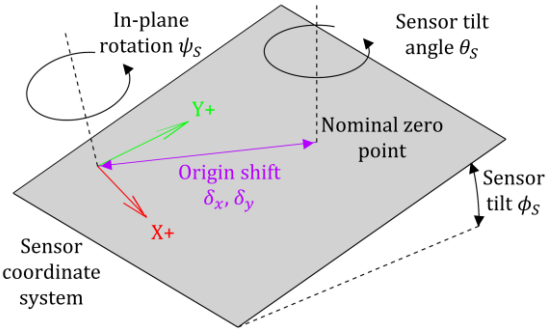

Fig. 3. PSM sensor plane tilt and alignment. The nominal zero point is the position that a laser which is perfectly coaxial to the spindle axis would impact the PSM plane when the machine is at (X0, Y0, Z0). The output voltages V_x, V_y are based on the laser incident point position in the sensor coordinate system.

The point where the laser beam coincides with the sensor is calculated by modeling the laser as a line and the sensor as a plane. For a given machine position $\{X, Y, Z, \theta\}$, the laser line is defined as $x_L(z) = a_x z + b_x, y_L(z) = a_y z + b_y$ using the coefficients given by Equation (1). The PSM sensor is in a plane $z_P(x, y) = t_x x + t_y y$ with the coefficients in Equation (2).

$$\begin{aligned} a_x &= \cos\theta \tan\phi_1 + \sin\theta \tan\phi_2 + \tan(\phi_{0Y} + \phi_{1Y} Z), \\ a_y &= \sin\theta \tan\phi_1 + \cos\theta \tan\phi_2 + \tan(\phi_{0X} + \phi_{1X} Z), \\ b_x &= -(l + Z) a_x + X + \epsilon_1 \cos(\theta) - \epsilon_2 \sin(\theta), \\ b_y &= -(l + Z) a_y + Y + \epsilon_1 \sin(\theta) + \epsilon_2 \cos(\theta) \end{aligned} \tag{1}$$

$$t_x = \frac{\cos(\theta_S)}{\tan\left(\frac{\pi}{2} - \phi_S\right)}, t_y = \frac{\sin(\theta_S)}{\tan\left(\frac{\pi}{2} - \phi_S\right)} \quad (2)$$

These equations are solved for the intersection point (x_S, y_S) and incident angles $(\theta_{SX}, \theta_{SY})$ where the laser intersects the sensor, expressed in the sensor coordinate system (see Fig. 2b). Equation (3) calculates the sensor voltages from these intersection points. The c_x and c_y terms represent fit voltage coefficients for the sensor itself. Cubic terms were found to give a good fit for the sensor linearity. The sensor reading is also affected by form errors in the intermediate mirrors, which can shift the laser position by >15 µm. The lumped orientation model does not geometrically model these mirrors or their form errors. Instead, the θ_{SX}, θ_{SY} fitting terms adjust the voltage predictions based on the incident angle and spindle height to approximate errors due to mirror flatness. Linear terms are used to prevent over-fitting. These equations are repeated for the second sensor to give the voltage predictions $V_{x1}, V_{y1}, V_{x2}, V_{y2}$. The sensors share the laser and spindle alignment but have unique alignment and voltage coefficients.

$$\begin{aligned} V_x &= x_S c_{x1} + x_S^2 c_{x2} + x_S^3 c_{x3} + (\theta_{SX} - \bar{\theta}_{SX}) \cdot \\ &\quad (c_{\theta xx} + Z\, c_{\theta xxZ}) + (\theta_{SY} - \bar{\theta}_{SY}) \cdot \left(c_{\theta xy} + Z\, c_{\theta xyZ}\right), \\ V_y &= y_S c_y + y_S^2 c_{y2} + y_S^3 c_{y3} + (\theta_{SX} - \bar{\theta}_{SX}) \cdot \\ &\quad \left(c_{\theta yx} + Z\, c_{\theta yxZ}\right) + (\theta_{SY} - \bar{\theta}_{SY}) \cdot \left(c_{\theta yy} + Z\, c_{\theta yyZ}\right) \end{aligned} \quad (3)$$

The voltage coefficient and sensor alignment (including tilt angles and linear offset) were fit based on a training data set. PSM data was collected at 90 different machine positions while the spindle rotated at 180 revolutions/min (rpm, 3 Hz). One second of data was collected at each location, for a total of 90 seconds of calibration data. The slow rotation speed was selected to approximate pseudo-static spindle motion and avoid mechanical resonances. The static stage magnets applied negligible external forces (≪ 1 N) during this data set collection. The Z-axis was positioned from 0 mm to 457.2 mm in 50.8 mm increments, while the X and Y axes were positioned at -1.27 mm, 0 mm, and 1.27 mm, creating a 3 × 3 grid of locations at each Z-axis height. These ranges constrain the laser center to a 5 mm × 5 mm area on the PSM, reducing nonlinearities and ensuring that the full laser spot was contained on the sensor at all times. Fig. 4 illustrates this data collection process. Fig. 5 shows the collected calibration data.

Calibration was performed using 1 % of the calibration data set. The calibration process had two steps. First, the non-periodic terms were fit using a nonlinear least-squares model which minimized the residuals between the predicted and actual voltages. The fit variables include the mean laser runouts, PSM sensor positions and orientations, and voltage coefficients. Periodic spindle errors were then introduced by making the laser angular and translational runouts $\phi_1, \phi_2, \epsilon_1, \epsilon_2$ to be functions of the spindle rotation angle θ using Fourier series. The Fourier coefficients were calculated from the remaining voltage residuals using linear least-squares fitting. One hundred (100) harmonics were fit for each runout term. These periodic error terms do not move the centroid of the traced path and thus do not alter the non-periodic calibration.

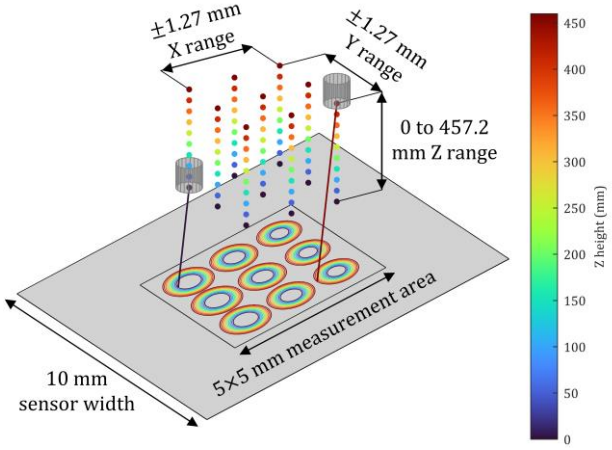

Fig. 4. Calibration data collection schematic, not to scale. Each colored dot represents a machine position where data was collected. The circles represent the paths traced by the laser as the spindle rotated, with the color indicating the Z height of the machine when that path was traced.

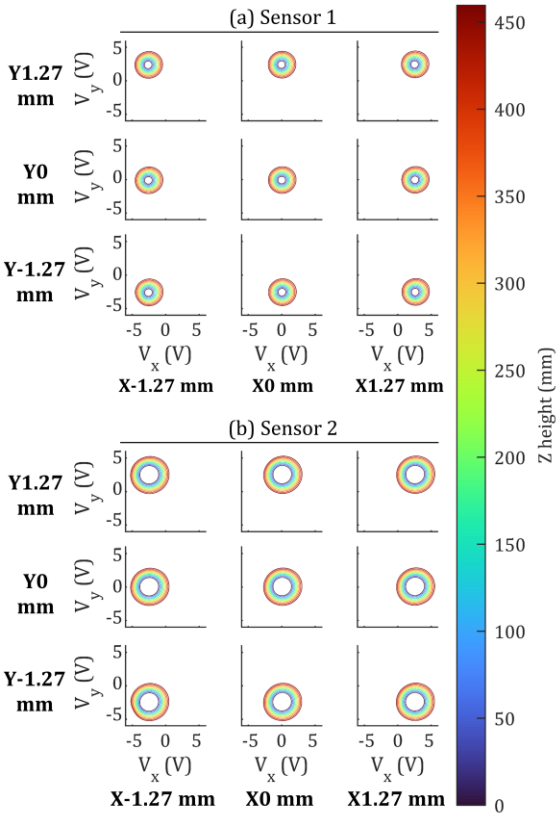

Fig. 5. Calibration data from both PSM sensors showing the path the laser traced out. (a) Sensor 1. (b) Sensor 2. The color indicates the Z height associated with the data. The sensor 1 traces are smaller than sensor 2 because the path length was shorter, so angular laser misalignments have less effect.

After calibration, the voltage predictions were validated against the full dataset. Table 1 shows the root mean square error (RMSE), mean absolute error (MAE), and maximum absolute error (MaxAE) for each voltage prediction. The fully calibrated model was generally able to capture the behavior of the laser. For example, Fig. 6 compares the radial deviations from a best fit circle for the sensor 1 readings, showing how the traced laser path deviates from a perfect circle. These roundness errors are caused by the tilt of the PSM sensor relative to the conical laser path, periodic spindle error motions,

and mirror form errors. While there are some variations, the model generally predicts the overall form of the roundness errors, indicating that it is correctly modelling the sensor orientation and periodic spindle errors. The largest out-of-round error was 0.056 V, corresponding to a displacement of approximately 28 µm. Local mirror form errors are believed to be the primary limiting factor for the prediction accuracy.

Table 1: Error metrics for the geometry model calibration. The equivalent errors in µm are calculated using the mean calibrated linear voltage coefficient of 1.975 V/mm.

Variable	Unit	Metric		
		MAE	RMSE	MaxAE
V_{x1}	mV	12.1	9.4	55.2
	µm	6.2	4.8	28.3
V_{y1}	mV	8.9	6.9	38.8
	µm	4.6	3.5	19.9
V_{x2}	mV	14.5	11.1	87.4
	µm	7.4	5.7	44.8
V_{y2}	mV	12.7	10.1	53.0
	µm	6.5	5.2	27.2

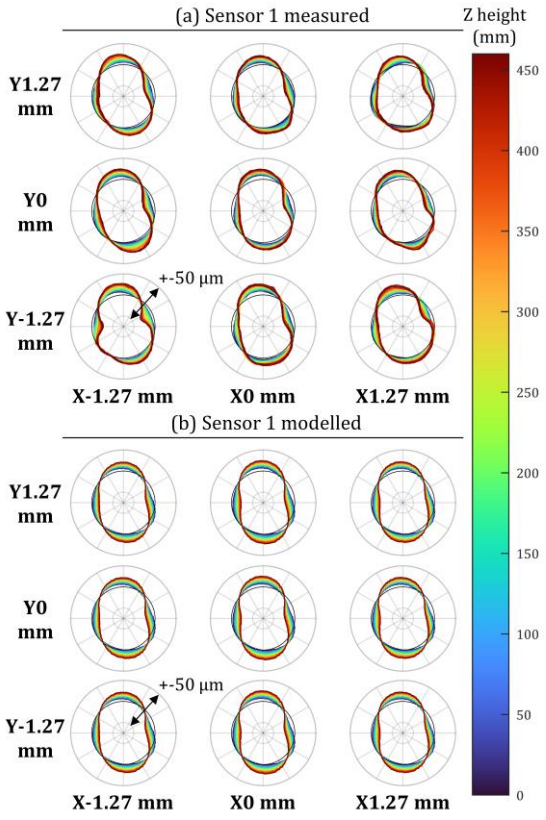

Fig. 6. (a) Measured roundness errors and (b) modeled roundness errors for the sensor 1 calibration data, calculated as radial deviations from the best-fit circle. Modeled errors were calculated with the calibrated geometry model. All plots use the same radial scale. Color indicates the Z height a trace was collected at.

The calibrated geometric model can then be used to calculate the spindle error motions E_{XC}, E_{YC}, E_{AC}, E_{BC} for data collected at a different spindle speed or with external forces, based on the deviation between the predicted and measured voltages at each timestep. Since the error motions are calculated relative to the pseudo-static predictions, they reflect deviations caused by external forces or speed-induced changes in spindle or laser behavior. Fig. 7 shows how the spindle error motions were used to update a prediction at 2500 rpm.

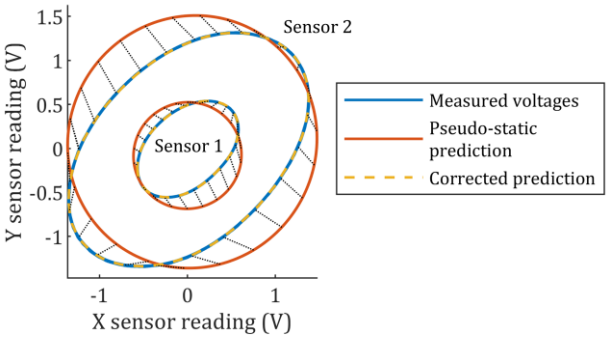

Fig. 7. Error motion fitting using the deviation between the pseudo-static and measured voltages. The black dotted lines show how a prediction is shifted with the addition of spindle error motions.

4. Spindle error displacement models

The spindle error motions determined by the method shown in Sec. 3 can now be related to the accelerations of the spindle housing. As outlined in Ref. [15], metrology suite data was collected in about 90 minutes for 1584 combinations of spindle speeds and magnetic force configurations with spindle speeds from 500 rpm to 7500 rpm and force ranges from about 1 N to about 200 N. Since the metrology suite is static, the calibrated geometry model will remain valid even at these higher speeds and loads. This “simulated cutting dataset” allowed for various data-driven approaches to model the dependence of the four tool holder laser-diode displacements (referred to here onwards as $\tilde{E}_{\mathrm{XC}}$, $\tilde{E}_{\mathrm{YC}}$, $\tilde{E}_{\mathrm{AC}}$, and $\tilde{E}_{\mathrm{BC}}$) on the three accelerations collected from one triaxial accelerometer [15].

In this work, the method shown in Sec. 3 transforms the four laser-diode displacements into the four relative spindle error motions before the removal of the least-squares circle [16]. These “relative spindle error displacements” ($\Delta\hat{E}_{\mathrm{XC}}$, $\Delta\hat{E}_{\mathrm{YC}}$, $\Delta\hat{E}_{\mathrm{AC}}$, and $\Delta\hat{E}_{\mathrm{BC}}$) represent the changes in the components of the translational or angular displacements of the laser-diode that are due to the spindle. This transformation process was applied for each of the 1584 data files. An individual model for each of the four spindle error displacements is then created, which takes the three accelerations as inputs and outputs the given spindle error displacement. Specifically, the same physics-inspired (PI) model and XGboost machine learning (ML) model [14] employed in Ref. [15] were used to model the relative spindle error displacements based on the transformed training data. This provides a fair comparison of model predictions of both types of displacements.

5. Spindle performance as a function of spindle speed

Fig. 8 shows the PI-modeled synchronous (i.e., average) laser-diode displacements ($\tilde{E}_{\mathrm{XC}}$, $\tilde{E}_{\mathrm{YC}}$, $\tilde{E}_{\mathrm{AC}}$, and $\tilde{E}_{\mathrm{BC}}$) and modeled synchronous relative spindle error displacements ($\Delta\hat{E}_{\mathrm{XC}}$, $\Delta\hat{E}_{\mathrm{YC}}$, $\Delta\hat{E}_{\mathrm{AC}}$, and $\Delta\hat{E}_{\mathrm{BC}}$) as functions of the spindle speed from 0 rpm to 6000 rpm. As seen in Fig. 1(a,b) and reported in Ref. [1, 15], radial and tilt misalignments of about 100 µm and 1.6 mrad, respectively, exist for the laser diode

when the spindle is stationary (0 rpm). The geometric model explained in Sec. 3 attempts to model these misalignments for the quasi-static spindle and then applies these same misalignments when the spindle is rotating, so that any changes in the laser-diode displacements in Fig. 8 (a,b) are assumed to be from the spindle error displacements seen in Fig. 8(c,d). Since the laser-diode displacements Fig. 8(a,b) are generally significantly greater than the relative spindle error displacements seen in Fig. 8(c,d), the geometric model reveals that the majority of the laser-diode displacements are from misalignments instead of spindle error displacements.

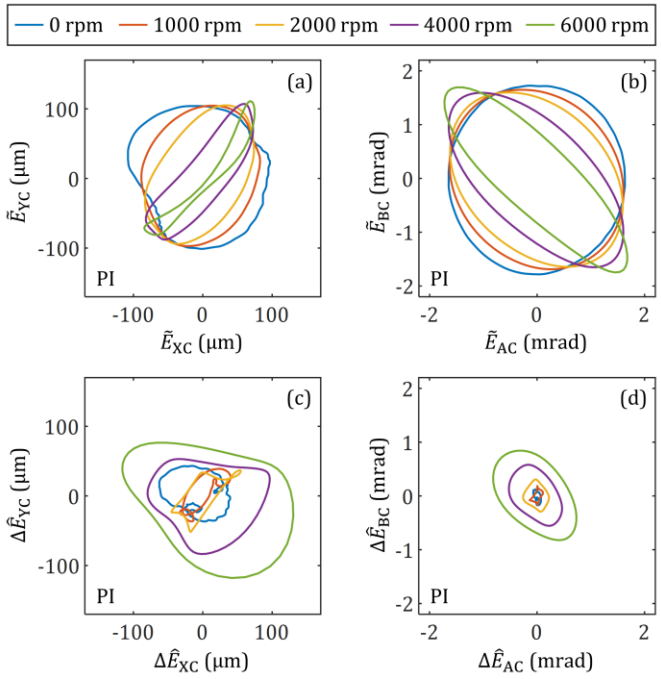

Fig. 8. Modeled synchronous laser-diode displacements, (a) $\tilde{E}_{XC}$ and $\tilde{E}_{YC}$ and (b) $\tilde{E}_{AC}$ and $\tilde{E}_{BC}$, and modeled synchronous relative spindle error displacements, (c) $\Delta\hat{E}_{XC}$ and $\Delta\hat{E}_{YC}$ and (d) $\Delta\hat{E}_{AC}$ and $\Delta\hat{E}_{BC}$. All responses are filtered to remove frequencies > 500 Hz since those terms are not modeled.

6. Comparison of model prediction performance metrics

Table 2 shows the prediction performance metrics of the models for the four relative spindle error displacements. The error metrics are the MAE, RMSE, and MaxAE of the metric populations for all 1584 data files [15]. As shown in Table 2, the PI models estimate $\Delta\hat{E}_{XC}$, $\Delta\hat{E}_{YC}$, $\Delta\hat{E}_{AC}$, and $\Delta\hat{E}_{BC}$ with average MAEs within about 2 % to 3.5 % of the respective mean ranges (M-Rs). In contrast, the XGB models have average MAEs that are within about 6 % to 7.5 % of the respective M-Rs. Thus, the PI models are roughly twice to three times more accurate than the ML models. Furthermore, the variances (ratios of the standard deviations to the means) of the PI-based error metrics are roughly 40 % of those for the XGB-based metrics, demonstrating that the PI models have better prediction performance for the PI models.

Similarly, Fig. 9 compares the ranges of the four modeled and measured relative spindle error displacements for the PI models in Fig. 9(a,b) and the XGB models in Fig. 9(c,d) for the simulated cutting dataset. As seen in the metrics listed in Table 2, the models are not perfect, so the plot markers do not generally coincide with the dashed identity lines. Nonetheless, the PI-modeled ranges nominally match the measured ranges, which is needed for process monitoring purposes.

Table 2. Prediction performance metrics for the PI and XGB models. The metrics have the form of "mean ± standard deviation."

Disp.	Model	Metric			M-R
		MAE	RMSE	MaxAE	
$\Delta\hat{E}_{XC}$ (µm)	PI	6.17 ± 2.34	7.21 ± 2.68	13.2 ± 4.77	173
	XGB	12.8 ± 5.96	15.0 ± 6.68	28.7 ± 11.3	
$\Delta\hat{E}_{YC}$ (µm)	PI	4.03 ± 1.87	4.56 ± 2.01	7.89 ± 2.97	142
	XGB	10.9 ± 4.38	12.9 ± 4.90	25.4 ± 8.98	
$\Delta\hat{E}_{AC}$ (µrad)	PI	30.5 ± 17.3	34.2 ± 19.1	53.2 ± 26.8	1010
	XGB	62.2 ± 34.6	71.6 ± 37.8	127 ± 56.1	
$\Delta\hat{E}_{BC}$ (µrad)	PI	21.1 ± 10.2	24.3 ± 11.3	42.9 ± 18.1	1110
	XGB	64.8 ± 37.3	74.5 ± 41.2	130 ± 62.1	

7. Comparison of model predictions

Fig. 10 compares the measured, PI-modeled, and XGB-modeled relative spindle error displacements for the cases with the lowest (< 10 N) and the highest (> 140 N) X-axis magnetic force range as the spindle speed increases from 500 rpm to 5500 rpm. The PI models generally outperform the XGB models in predicting the measured trajectories. Nonetheless, both models are nominally able to predict how spindle speeds and external forces (via accelerations) alter the error displacements. Each PI model has 2211 trainable FRF parameters, while each XGB model has up to 12700 nodes, with all models having the potential for improvements through more training data.

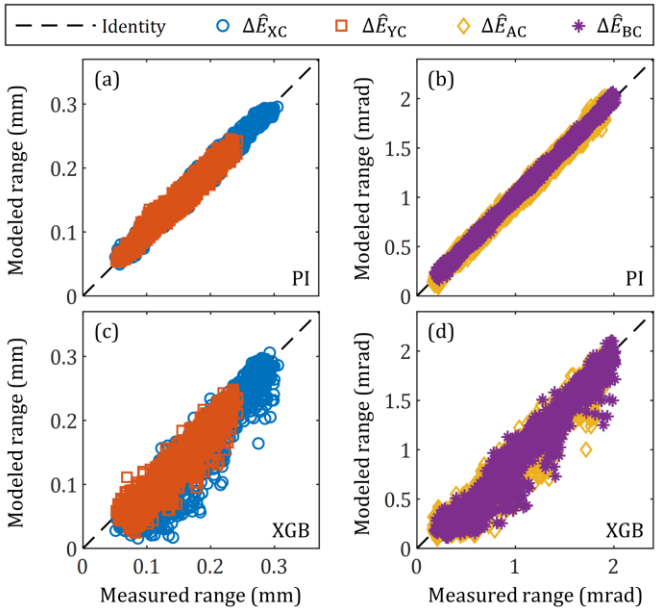

Fig. 9. Modeled displacement range versus the measured displacement range for all simulated cutting tests, using the PI models for (a) $\Delta\hat{E}_{XC}$ and $\Delta\hat{E}_{YC}$ and (b) $\Delta\hat{E}_{AC}$ and $\Delta\hat{E}_{BC}$ and the XGB models for (c) $\Delta\hat{E}_{XC}$ and $\Delta\hat{E}_{YC}$ and (d) $\Delta\hat{E}_{AC}$ and $\Delta\hat{E}_{BC}$.

8. Conclusions

A method was described for estimating error motions from using spindle-mounted accelerometers. Spindle motions were recorded by measuring the deflection of a spindle-mounted laser beam during spindle rotation while the tool holder encounters periodic magnetic forces. Training data were preprocessed using a geometric model that isolates externally induced translational and rotational spindle errors. The processed training data were used to train two different data-driven models, a physics-inspired model and a machine learning model, to predict spindle error motions based on accelerometer readings. Future work will focus on validating the identified spindle errors using capacitance probes at a variety of spindle speeds, further compensating for optical nonlinearities in the system to improve the calibration model, using the measured error motions for spindle health diagnosis, and evaluating the identified spindle-speed dependent FRFs.

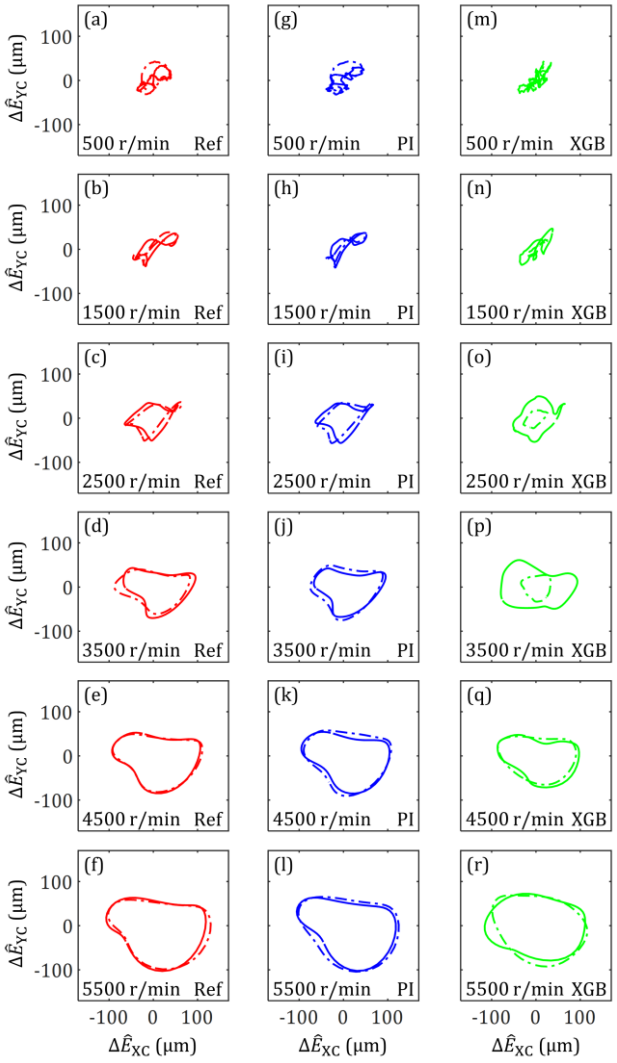

Fig. 10. (a-f) Measured, (g-l) PI-modeled, and (m-r) XGB-modeled relative spindle error displacements, $\Delta\hat{E}_{XC}$ and $\Delta\hat{E}_{YC}$, for spindle speeds from 500 rpm to 5500 rpm. At each speed, the responses for two different cases are contrasted: dash-dotted curves are for the case with the lowest X-, Y-, and Z-axis magnetic force ranges (< 10 N), while solid curves are for the case with the highest X-axis magnetic force range (> 140 N).

Acknowledgements

The authors thank the Fabrication Technology Office at NIST for their significant contributions towards the experimental setup.

NIST disclaimer

Certain commercial equipment, instruments, or materials are identified in this paper in order to specify the experimental procedure adequately. Such identification is not intended to imply recommendation or endorsement by NIST, nor is it intended to imply that the materials or equipment identified are necessarily the best available for the purpose. This material is declared a work of the U.S. Government and is not subject to copyright protection in the United States. Approved for public release; distribution is unlimited.

References

[1] International Organization for Standardization (ISO). ISO 230-7 - Test Code for Machine Tools − Part 7: Geometric Accuracy of Axes of Rotation. 2015.
[2] Cao H, Li B, He Z (2012) Chatter Stability of Milling with Speed-Varying Dynamics of Spindles. *International Journal of Machine Tools and Manufacture* 52(1):50-58.
[3] Cao H, Zhang X, Chen X (2017) The Concept and Progress of Intelligent Spindles: A Review. *International Journal of Machine Tools and Manufacture* 112:21-52.
[4] Grossi N, Sallese L, Scippa A, Campatelli G (2017) Improved Experimental-Analytical Approach to Compute Speed-Varying Tool-Tip Frf. *Precision Engineering* 48:114-122.
[5] Zhang H, Anders D, Löser M, Ihlenfeldt S, Czarske J, Kuschmierz R (2020) Non-Contact, Bi-Directional Tool Tip Vibration Measurement in CNC Milling Machines with a Single Optical Sensor. *Mechanical Systems and Signal Processing* 139:106647.
[6] Postel M, Aslan D, Wegener K, Altintas Y (2019) Monitoring of Vibrations and Cutting Forces with Spindle Mounted Vibration Sensors. *CIRP Annals* 68(1):413-416.
[7] Spiewak SA, Nickel T (2001) Vibration Based Preload Estimation in Machine Tool Spindles. *International Journal of Machine Tools and Manufacture* 41(4):567-588.
[8] Oh L, Pitz E, Pochiraju K (2023) Spindle Condition Monitoring with a Smart Vibration Sensor and an Optimized Deep Neural Network. *Journal of Nondestructive Evaluation, Diagnostics and Prognostics of Engineering Systems* 6(2):021003.
[9] Nawrocki W, Stryjski R, Kostrzewski M, Woźniak W, Jachowicz T (2023) Application of the Vibro-Acoustic Signal to Evaluate Wear in the Spindle Bearings of Machining Centres. In-Service Diagnostics in the Automotive Industry. *Journal of Manufacturing Processes* 92:165-178.
[10] Tai C-Y, Altintas Y (2024) A Physics-Based Model-Data-Driven Method for Spindle Health Diagnosis, Part I: Modeling of Geometric Faults. *Journal of Manufacturing Science and Engineering* 146(8):081004.
[11] Zhou J, Mao X, Liu H, Li B, Peng Y (2018) Prediction of Cutting Force in Milling Process Using Vibration Signals of Machine Tool. *The International Journal of Advanced Manufacturing Technology* 99(1-4):965-984.
[12] Liu Y-P, Altintas Y (2022) Transmissibility Enhanced Inverse Chatter Stability Solution. *Journal of Manufacturing Science and Engineering* 144(1):1-41.
[13] Liu Y-P, Altintas Y (2021) In-Process Identification of Machine Tool Dynamics. *CIRP Journal of Manufacturing Science and Technology* 32:322-337.
[14] Chen T, Guestrin C. Xgboost: A Scalable Tree Boosting System. Proceedings of the 22nd ACM SIGKDD International Conference on Knowledge Discovery and Data Mining: ACM; 2016. pp. 785-794.
[15] Vogl GW, Rahman MW, Qu Y. Spindle Performance Monitoring Via Accelerometer Measurements in Data-Driven Models. 18th CIRP Conference on Intelligent Computation in Manufacturing Engineering (CIRP ICME). Gulf of Naples, IT2024. pp. 318-323.
[16] Vogl GW, Regli DA, Corson GM (2022) Real-Time Estimation of Cutting Forces Via Physics-Inspired Data-Driven Model. *CIRP Annals* 71(1):317-320.